arXiv:2008.10628v3 [cond-mat.str-el] 14 Jan 2021

Prediction of Spin Polarized Fermi Arcs in Quasiparticle Interference of CeBi

Zhao Huang,[1] Christopher Lane,[1,2] Chao Cao,[3] Guo-Xiang Zhi,[4] Yu Liu,[5] Christian E. Matt,[5] Brinda Kuthanazhi,[6,7] Paul C. Canfield,[6,7] Dmitry Yarotski,[2] A. J. Taylor,[2] and Jian-Xin Zhu[1,2,*]

[1]*Theoretical Division, Los Alamos National Laboratory, Los Alamos, New Mexico 87545, USA*
[2]*Center for Integrated Nanotechnology, Los Alamos National Laboratory, Los Alamos, New Mexico 87545, USA*
[3]*Department of Physics, Hangzhou Normal University, Hangzhou 310036, China*
[4]*Department of Physics, Zhejiang University, Hangzhou 310013, China*
[5]*Department of Physics, Harvard University, Cambridge, Massachusetts 02138, USA*
[6]*Ames Laboratory, Iowa State University, Ames, Iowa 50011, USA*
[7]*Department of Physics and Astronomy, Iowa State University, Ames, Iowa 50011, USA*

(Dated: January 22, 2022)

We predict that CeBi in the ferromagnetic state is a Weyl semimetal. Our calculations within density functional theory show the existence of two pairs of Weyl nodes on the momentum path $(0,0,k_z)$ at 15 meV above and 100 meV below the Fermi level. Two corresponding Fermi arcs are obtained on surfaces of mirror-symmetric (010)-oriented slabs at $E = 15$ meV and both arcs are interrupted into three segments due to hybridization with a set of trivial surface bands. By studying the spin texture of surface states, we find the two Fermi arcs are strongly spin-polarized but in opposite directions, which can be detected by spin-polarized ARPES measurements. Our theoretical study of quasiparticle interference (QPI) for a nonmagnetic impurity at the Bi site also reveals several features related to the Fermi arcs. Specifically, we predict that the spin polarization of the Fermi arcs leads to a bifurcation-shaped feature only in the spin-dependent QPI spectrum, serving as a fingerprint of the Weyl nodes.

I. INTRODUCTION

Despite being predicted more than 90 years ago as an elegant special solution of the relativistic wave equation, Weyl fermions have never been observed in nature. However, just as the sun was setting on the Weyl fermion, they were observed as a quasiparticle in the electronic structure of TaAs, thereby pushing Weyl physics back to the vanguard and invigorating the search for other exotic relativistic particles within solids. Weyl fermions appear in condensed matter systems when a single Dirac cone is split into two by the breaking of either time-reversal[1–6] or inversion symmetry[7–13]. This process generates a pair of cone-like features with opposite chirality defined by their Berry curvature[14]. As a direct consequence, anomalous surface states appear connecting Weyl nodes of opposite topological charge, providing an experimentally accessible fingerprint of the underlying non-trivial band topology[4,15–21].

Recently, magnetic Weyl semi-metals have been gaining interest for providing a new platform to study the interplay between chirality, magnetism, correlation, and topological order, thus opening up new routes to novel quantum states, spin polarized chiral transport[22,23], and exotic optical phenomena[24–27]. Compared with inversion breaking Weyl materials, magnetic Weyl materials have the advantage of reducing the minimum number of allowed Weyl nodes from four to two. This allows simpler band structures thereby facilitating clearer comparisons with theoretical predictions, and more robust applications in spintronics[28–30] and quantum computation[31–34]. Another advantage is the magnetic field tunability which provides us a strong tool on controlling the band structure and related electromagnetic functionality.

To date very few magnetic Weyl materials have been synthesized, demonstrating an urgent and important need for more theoretical material predictions and robust growth protocols. Only very recently have $Co_3Sn_2S_2$ and Co_2MnGa been reported as possible magnetic Weyl semimetals with six Weyl nodes and nodal lines, respectively[4–6]. This is far from enough to explore the wide range of possible exotic states. Interestingly, recent experimental reports of a pronounced negative magnetoresistance and observed band inversion in cerium monopnictides[35–37] and the geometrically frustrated Shastry-Sutherland lattice GdB_4[38] could provide clues to a possible new material family harboring Weyl physics.

In this paper, we argue that CeBi in the ferromagnetic (FM) state is a magnetic Weyl semimetal using first-principles LDA+U calculations and we predict robust quasiparticle interference (QPI) signatures of spin polarized Fermi arcs directly accessible by spin resolved scanning tunneling spectroscopy (STS). By aligning the Ce magnetic moments along the c-axis, we find two pairs of Weyl nodes on the zone diagonal along the k_z-axis at 15 meV above and 100 meV below the Fermi level. Then by examining a (010)-oriented slab which is mirror symmetric, two Fermi arcs of opposite spin polarization are observed on both the top and bottom of surfaces, stretching across the Brillouin zone. These Fermi arcs then hybridize with a set of trivial surface states producing a spin vortex encircling the $\bar{M}$ point in the Brillouin zone. Finally, by considering a weak potential scatterer at the Bi site on the surface, we predict several features directly related to the scattering among the Fermi arcs in the QPI spectra. Specifically, there is a bifurcation-shaped feature originating from the scattering between the two symmetric outer segments of the spin-up Fermi arc. We propose this feature as a direct indicator of the Weyl nodes for future experiments. Moreover, due to the isolation of the Weyl nodes near the Fermi level, we find CeBi to be a robust platform for theoretical and experimental analysis of Weyl physics with minimal interference from trivial bulk states.

II. METHOD

First-principles band structure calculations were carried out within density functional theory framework using the generalized-gradient approximation (GGA) as implemented in the all-electron code WIEN2K[39], which is based on the augmented-plane-wave + local-orbitals(APW+lo) basis set. Spin-orbit coupling was included in the self-consistency cycles. Furthermore, the Hubbard Coulomb interaction on Ce-4f electrons was incorporated to ensure a fully localized Ce-4f state, which also gives a total magnetic moment of $2\mu_B$/Ce consistent with earlier studies oncerium monopnictides[35,40,41]. Although these compounds exhibit several field-induced magnetic phases, a ferromagnetic-like state can be stabilized using state-of-the-art cryogenic STM in 3D vector magnetic fields above 4 Tesla[35,41,42]. The topological analysis was performed by employing a real-space tight-binding model Hamiltonian, which was obtained by using the wien2wannier interface[43]. Bi-6p and Ce-5d states were included in generating Wannier functions. It is worth mentioning that, the DFT+U method for a non-magnetic phase will still leave f-electron pinned around the Fermi level, which is completely different from the spin-polarized case[44]. Therefore, the DFT+U approach is not appropriate to describe strongly correlated materials in a paramagnetic state, for which one needs to resort to more powerful methods like DFT+DMFT.[45]

To identify the presence of a pair of Weyl nodes in a given band structure we must check if the band crossings are topologically trivial or non-trivial. That is, we must calculate the Berry curvature at and surrounding the nodal points to see if the field is divergent or not. To do so, we calculate the Berry curvature $\Omega_{n,\alpha\beta}(\mathbf{k})$ as implemented in the WannierTools package[46–48], for a given band n and momenta $\mathbf{k}$ as

$$\Omega_{n,\alpha\beta}(\mathbf{k}) = -2\mathrm{Im}\sum_{m\neq n}\frac{v_{nm,\alpha}(\mathbf{k})v_{mn,\beta}(\mathbf{k})}{[\varepsilon_{m\mathbf{k}}-\varepsilon_{n\mathbf{k}}]^2} \quad (1)$$

where $\varepsilon_{n\mathbf{k}}$ is the eigenvalue of Hamiltonian H for band n and momenta $\mathbf{k}$ and the matrix elements of the Cartesian velocity operators are given by

$$v_{nm,\alpha}(\mathbf{k}) = \langle\phi_{n\mathbf{k}}\left|\frac{\partial\hat{H}(\mathbf{k})}{\partial k_\alpha}\right|\phi_{m\mathbf{k}}\rangle\,. \quad (2)$$

Finally the Berry curvature vector is given by

$$\Omega_{n,\gamma}(\mathbf{k}) = \varepsilon_{\alpha\beta\gamma}\Omega_{n,\alpha\beta}(\mathbf{k}) \quad (3)$$

where $\varepsilon_{\alpha\beta\gamma}$ is the Levi-Civita tensor.

The surface electronic structure was calculated using both the direct diagonalization and the iterative Green's function method[49,50]. The QPI spectra was obtained within the T-matrix approximation as given by:

$$\mathrm{QPI}(\mathbf{q},\omega) = i(2\pi)^{-1}\int d^2\mathbf{k}(2\pi)^{-2}[B(\mathbf{q},\omega)-B^*(-\mathbf{q},\omega)], \quad (4)$$

where $B(\mathbf{q},\omega) = \mathrm{Tr}[G(\mathbf{k}+\mathbf{q},\omega)\mathbf{T}(\omega)G(\mathbf{k},\omega)]$ with $\mathbf{q}$ and ω the scattered wave vector and quasiparticle energy, respectively. G is the spin-dependent matrix surface Green's function composed of 6 Bi-6p and 10 Ce-5d orbitals, and $\mathbf{T}$ is the scattering T-matrix containing all multiple scattering effects off a single-site impurity. Since the infinite sum of multiple scattering terms form a geometric series, the T-matrix can be compactly written as $\mathbf{T}(\omega) = \left[\mathbf{I}-\mathbf{V}_{imp}(2\pi)^{-2}\int d^2\mathbf{k}G(\mathbf{k},\omega)\right]^{-1}\mathbf{V}_{imp}$, where $\mathbf{V}_{imp}$ is the impurity potential. Here we considered a Born approximation of the impurity scattering such that $\mathbf{T} = \mathbf{V}_{imp}$ and further chose $\mathbf{V}_{imp}$ to be a constant diagonal matrix with non-zero elements only for p (d) orbitals for a Bi (Ce) impurity site. Our general methodology for QPI prediction in CeBi is justified by the good agreement between calculated and experimental STS data on the (001)-oriented slab, shown in detail in the Supplemental Material (SM)[50].

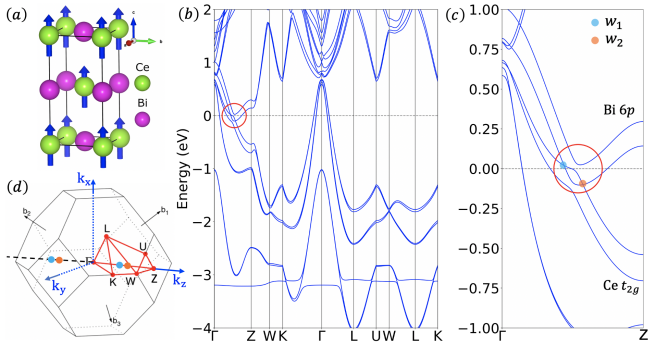

FIG. 1. (a) Crystal structure of CeBi with the spin polarization along the c-axis direction. Here we display a body-centered tetragonal cell for an otherwise FCC crystal structure of CeBi in bulk. (b) DFT electronic band structure of CeBi in the ferromagnetic state with a red circle highlighting a pair of Weyl nodes near the Fermi level. (c) Same as (b) except a zoom-in around Fermi level along $\Gamma-Z$ with the character of various bands indicated. (d) FCC Brillouin zone of FM CeBi with the various high-symmetry points marked. The locations of the Weyl nodes is given by teal (orange) dots denoting the Weyl node as a source (sink) of Berry curvature.

III. BAND STRUCTURE AND WEYL NODES

Figure 1 (left panel) shows the crystal structure of CeBi in the FM phase along with its corresponding face-centered-cubic (FCC) Brillouin zone, where various high symmetry lines are marked. The middle panel presents the electronic band dispersions evaluated over the full set of high symmetry points. The energy bands near the Fermi level are mainly of Bi-6p and Ce-5d character. Moreover, the moment-carrying localized Ce-4f states, which provides an effective Zeeman exchange field, are seen as a flat band at 3 eV binding energies. We choose $U = 7.9$ eV and $J = 0.69$ eV in our *ab initio* calculations to make the Ce-4f energy level consistent with the corresponding state in CeSb as reported by photoemission spectroscopy[51]. Moreover, the non-trivial topological nature of low-energy states in CeBi are not sensitive to the value of U once Ce-4f electrons are quite localized in the ferromagnetic phase.

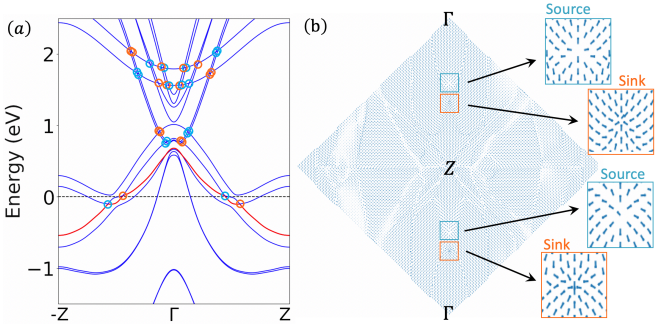

FIG. 2. Electronic band structure of CeBi in the FM phase along $-Z-\Gamma-Z$ in the Brillouin zone. The band that passes through the Weyl nodes near the Fermi level is shown in red. (b) Berry curvature vector field in the xz-plane for the red band in (a). The Weyl nodes are marked in teal (orange) indicating they are a source (sink) of Berry flux.

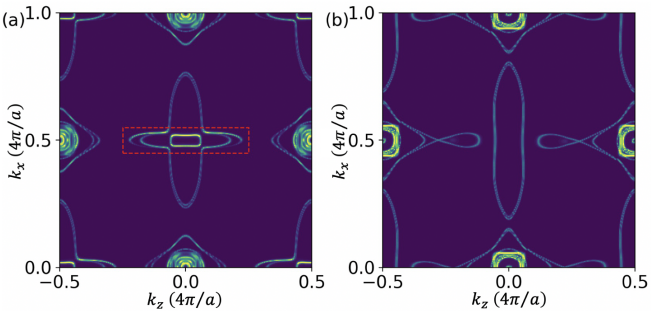

FIG. 3. Surface projected spectral function of the bottom layer of 10-layer (010)-oriented slab (a) and the corresponding bulk (b).

The most important feature of the band structure is the pair of Weyl nodes that appears along $\Gamma-Z$ at the Fermi level. These two Weyl nodes are formed by the crossing of Bi-6p and Ce-5d t_{2g} orbital character bands that have been spin split by the internal Zeeman exchange field [Fig. 1 (right panel)]. The Weyl nodes w_1 and w_2 are located at $(0,0,0.22)\frac{4\pi}{a}$ and $(0,0,0.28)\frac{4\pi}{a}$ in the Brillouin zone and at 15 meV above and 100 meV below the Fermi level, respectively. Here a is the lattice constant of the cubic conventional cell and hereafter we will choose $4\pi/a=1$. Due to mirror symmetry in the xy-plane, a duplicate pair of Weyl nodes are found along the $-k_z$ axis, named as $\bar{w}_1$ and $\bar{w}_2$. The locations of these four Weyl nodes are marked in the Brillouin zone [Fig. 1 (left panel)] by the teal (orange) dots, where the teal (orange) color indicates a Weyl node as a source (sink) of Berry curvature. Importantly, since the Weyl nodes in CeBi are isolated near the Fermi level, the experimental signatures and theoretical analysis will be less obstructed as compared to $Co_3Sn_2S_2$ and Co_2MnGa.

Figure 2(a) shows w_1 and w_2 near the Fermi level along the $-Z-\Gamma-Z$ cut in the Brillouin zone. The band that passes through the Weyl nodes is marked in red. Figure 2(b) shows the corresponding Berry curvature vector field in the xz-plane of the first Brillouin zone for the red band in Fig. 2(a). Two clear divergences in the vector field are seen along $\pm Z-\Gamma$ at the Weyl nodes, with one node as a source (teal) and the other a sink (orange) of topological charge. This confirms the topologically non-trivial nature of these Weyl band crossings. Furthermore, we identified 16 additional pairs of Weyl node existing above the Fermi energy, each marked in Fig. 2(a) by an orange or teal circle denoting its topological charge.

IV. SURFACE SPECTRAL FUNCTIONS

Due to the presence of Weyl nodes near the Fermi level we expect the emergence of a pair of Fermi arcs connecting nodes of opposite topological charge when CeBi is cleaved along a given crystal plane exposing a surface. However, the situation is more subtle in magnetic Weyl materials. Since the internal magnetic moments on the Ce atoms point in the c-axis direction, the irreducible group elements are different for a (010)-oriented surface compared to those for a (001)-oriented surface. Specifically, the (001)-oriented surface breaks the xy mirror symmetry and k_z is no longer a good quantum number, whereas a (010)- or (100)-oriented surface preserves the symmetry. Furthermore, a (001)-oriented surface will not reveal Fermi arcs since the pairs of Weyl nodes with opposite chirality are projected to the same point on the surface, thus cancelling each other, while a (010) or (100)-oriented surface is expected to produce the Fermi arcs. Here we focus on the (010)-oriented surface and examine the resulting electronic structure and effect of the Fermi arcs on the QPI spectrum.

To distinguish the topologically non-trivial surface states and the trivial surface bands derived from the bulk, we consider the band structure of a 10-layer (010)-oriented slab, and also the bulk with supercell containing 10 layers of CeBi along the same direction. The spectral functions for the bottom layer of both cases are presented in Fig. 3. By comparing the two panels, we can see that all bands in Fig. 3(a) except for the Fermi arcs [highlighted in the red frame] have the corresponding bulk bands in Fig. 3(b). This indicates that the Fermi arcs are the non-trivial topology induced edge states. The massless energy bands corresponding to Fermi arcs are shown in the supplementary[50].

Figure 4(a) shows the surface spectral function $A_{\rm surf}(\mathbf{k},\omega)$ for an effective 64-layer (010)-oriented slab in the surface reciprocal space, centered at the $\bar{M}$ point, for a constant-energy cut of ω corresponding to w_1. Two clear Fermi arcs are seen connecting projections of the Weyl nodes w_1 to $\bar{w}_1$ and w_2 to $\bar{w}_2$, labeled as arc I and arc II, respectively. By breaking down the spectral function into its orbital components, we find the Fermi arcs to be mainly composed of Bi p_x and p_y, and Ce t_{2g} orbitals. The dominant Bi p_x and weaker Bi p_z contribution, along with their spin dependence, is given in Fig. 4(b).

Interestingly, as the two Fermi arcs traverse across the Brillouin zone they are intersected by and hybridize with two majority p_z character trivial bands extending along the k_x direction [Fig. 4(a)]. The avoided crossing between these two sets of bands yields a nearly continuous outer cross shaped Fermi surface and a rectangular pocket surrounding $\bar{M}$. More-

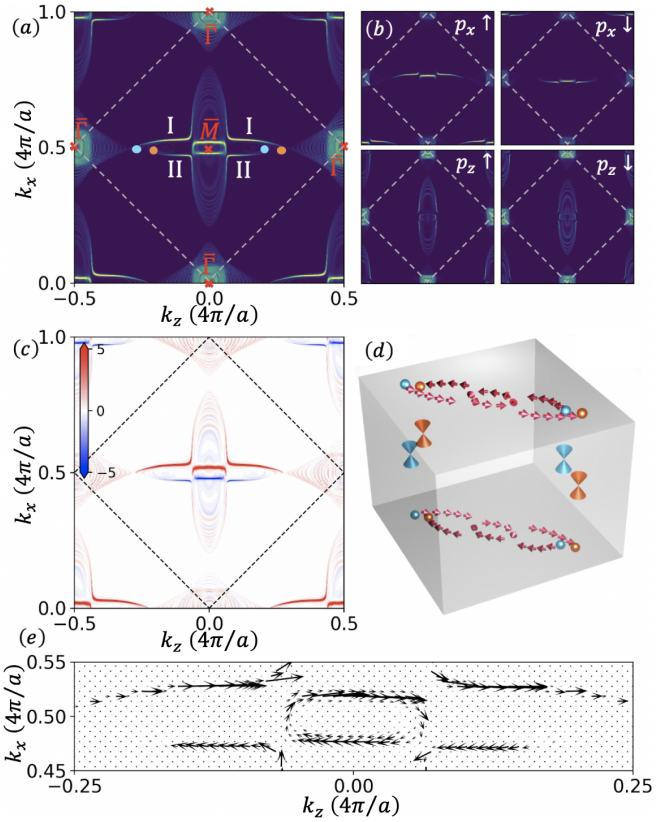

FIG. 4. ((a) Surface spectral function of a (010)-oriented surface of FM CeBi. The dash lines draw the boundary of the surface first Brillouin zone. I and II denotes the two Fermi arcs connecting the Weyl nodes. (b) Spin- and orbital-resolved surface spectral functions. (c) Spin polarization $\langle S_z \rangle$ in the Brillouin zone. (d) Schematic of the spin texture of various Fermi arcs in the Brillouin zone. (e) Calculated spin texture of the Fermi arcs.

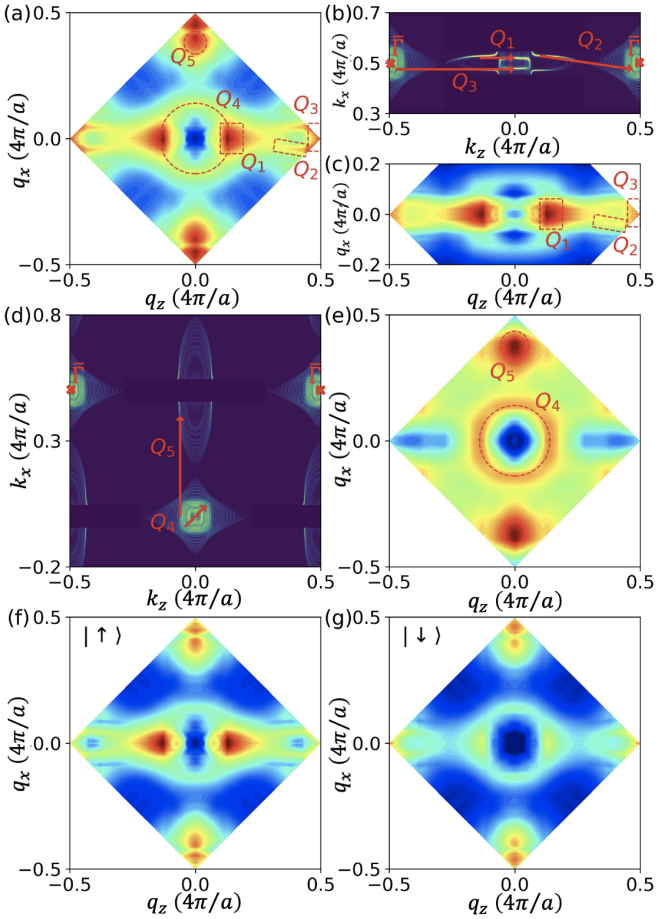

FIG. 5. (a) QPI spectra for a (010)-oriented surface of FM CeBi with the dominant scattering vectors indicated. (b) Surface spectral function with the trivial p_z states removed with various characteristic scattering transitions marked. (c) QPI spectra corresponding to the surface spectral function in (b). (d) Surface spectral function with Fermi arcs and spin vortex removed, with dominant scattering vectors indicated. (e) QPI spectra corresponding to the surface spectral function in (d). QPI spectra of the spin-up (f) and spin-down channel (g) corresponding to the surface spectral function in Fig. 4(a).

over, additional trivial surface states are observed around the $\bar{\Gamma}$ point, but they do not interact with the arcs.

Figure 4(c) shows $\langle s_z(\mathbf{k},\omega)\rangle = -\frac{1}{\pi}\mathrm{ImTr}[\sigma_3 G(\mathbf{k},\omega)]$ in the first Brillouin zone for a constant-energy cut of $\omega = w_1$, where red (blue) indicates the strength of the positive (negative) σ_3 projection of the surface spectral function. Here we find arc I and arc II to be oppositely spin polarized, which is also reflected in Fig. 4(b). This is the consequence of the spin-momentum locking effect around the $\bar{M}$ point which originates from the strong spin-orbital coupling in CeBi. Moreover, the strength of polarization is generically greater for arc I compared to arc II, due to the FM order along the c-axis.

Figure 4(d) and (e) show the full spin texture of the Fermi arcs in the (010)-oriented slab. We note several important features: (i) Arc I is strongly polarized along $+z$, whereas arc II is strongly polarized along $-z$. (ii) Due to inversion symmetry, the spin polarization for a given (k_z,k_x) on the bottom surface is equivalent to the spin polarization on the top surface at $(-k_z,-k_x)$. (iii) The Fermi surface pocket surrounding $\bar{M}$ forms a spin vortex in the momentum space, owing to strong spin-orbit coupling. (iv) The spin-polarization vector lies completely in the (k_z,k_x) plane, where $\langle s_y\rangle$ is strictly zero. The absence of any out-of-plane spin polarization S_y is guaranteed by the combined symmetry of time-reversal symmetry T and twofold rotational symmetry along the y axis C_{2y}, even though T or C_{2y} itself is broken. This symmetry is satisfied the Hamiltonian of the (010) slab with $C_{2y}TH(k_x,k_z)T^{-1}C_{2y}^{-1} = H(k_x,k_z)$. Since T flips all spin components and reverses all crystal momenta, and C_{2y} only flips S_x,S_z and reverses k_z,k_x, the combined transformation $C_{2y}T$ maps (k_z,k_x) to itself and reverses S_y. Because $(C_{2y}T)^2 = 1$, there is no Kramers degeneracy, implying $C_{2y}T|k_z,k_x\rangle$ and $|k_z,k_x\rangle$ can only differ by a phase, forbidding different S_y. Therefore, the expectation value of S_y must be strictly zero throughout the Brillouin zone.

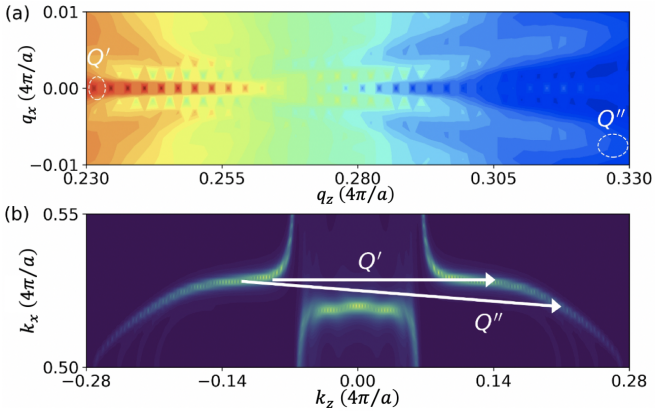

FIG. 6. (a) Zoom-in view of the QPI spectra in Fig. 5(a) highlighting the bifurcated feature corresponding to direct Fermi arc-Fermi arc scattering. (b) Close-up of the surface spectral function in Fig. 4(a) with scattering vectors Q' and Q" connecting the two outer segments of the spin-up Fermi arc.

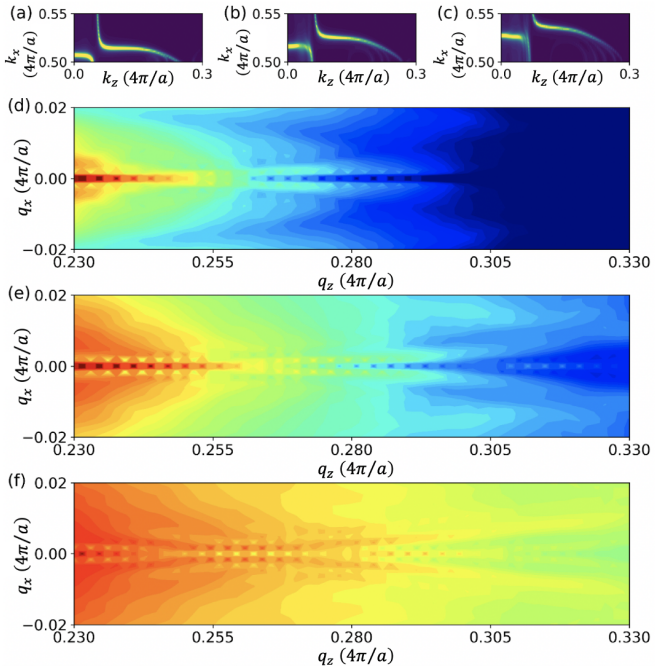

FIG. 7. Spectral function around one Fermi arc at (a) −50 meV, (b) 0 meV and (c) 50 meV. QPI spectra in the same regime as Fig. 4(a) at (d) −50 meV, (e) 0 meV and (f) 50 meV.

V. QUASIPARTICLE INTEREFERENCE

Bi-site impurity – At first we present our theoretical study on the (010)-oriented surface QPI derived from scattering between these surface states due to an isotropic nonmagnetic impurity at Bi site. Figure 5(a) shows the QPI spectra in the first Brillouin zone for a constant energy cut of $\omega = w_1$. Firstly, we notice that almost all $\mathbf{q} = 0$ scattering is suppressed by destructive interference between the various multi-orbital scattering channels. This phenomena is not present in the simple joint density of state description since the phase of wavefunctions is neglected. But because $\mathrm{QPI}(0,\omega) \propto \int d^2\mathbf{k}\mathrm{ImTr}[G(\mathbf{k},\omega)T(\mathbf{k},\omega)G(\mathbf{k},\omega)]$, the off diagonal components of the matrix Green's function contribute to the QPI signal. Moreover, the sign of the imaginary part of the product is highly sensitive to the relative sign between real and imaginary parts of the Green function and $\mathbf{k}$ in the Brillouin zone. Therefore, even after integrating over the full zone the results may be quite small. A similar cancellation takes place for scattering at finite $\mathbf{q}$, which leads to a quite broad and smooth QPI spectrum despite sharp features in the spectral function.

In Fig. 5(a) the five main features in the QPI pattern, corresponding to strong scattering between the surface states, are labeled with Q_1 through Q_5 and are highlighted by red dash circles and rectangles. In order to pinpoint the origin of the these strong features, we isolate various sections of the surface spectral function by masking out the Green function in other sections and amplify their effect on the QPI spectra. If we only consider the scattering between the Fermi arcs, spin vortex, and bands surrounding $\bar{\Gamma}$ [Fig. 5(b)] we find the Q_1, Q_2 and Q_3 features persist in the QPI [Fig. 5(c)]. Therefore, we find the momentum transfer Q_1 to connect the outer segment of the Fermi arc to the pocket surrounding $\bar{M}$. Q_2 scatters electrons from the outer segments of Fermi arcs to the trivial bands around $\bar{\Gamma}$. Because the Fermi arc is curved, a curved bridge-like dispersion is seen in the Q_2 rectangle. Q_3 transfers momentum between the Fermi pocket to the trivial bands around $\bar{\Gamma}$. If we now consider the spectral function in the region away from the Fermi arcs and spin vortex [Fig. 5(d)], we find the remaining Fermi sheets clearly produce the remaining features Q_4 and Q_5 [Fig. 5(e)]. Q_4 comes from the internal scattering of the bands around $\bar{\Gamma}$, whereas the Q_5 scattering vector connects p_z dominant states to those surrounding $\bar{\Gamma}$.

Since the surface spectral function exhibits a strong spin texture, it is reasonable to expect a highly spin dependent QPI. Figures 5(f)-(g) show the up and down-spin projection of the QPI spectra. These two patterns are quite similar except for scattering momenta related to Q_1. Since Q_1 connects Fermi arcs of the same $+z$ spin polarization, the intensity in the spin-up QPI channel is stronger than that in the spin-down channel. This stark difference in the spin-up and spin-down QPI maps provides a direct experimentally accessible prediction of the underlying spin-polarized Fermi arcs.

Thus far, we have covered all the strong scattering transitions in the QPI map. However, the scattering between the two outer Fermi arcs appears to be missing. There should be features in the QPI spectra corresponding to this scattering channel. Indeed, upon close inspection, a red flat tail can be seen at $(q_z, q_x) = (\pm 0.25, 0)$ in Figs. 5(a), 5(c) and 5(f) corresponding to this 'missing' scattering pathway. Figure 6(a) shows a zoomed in section of the QPI map given in Fig. 5(a) displaying a dispersing bifurcating feature. The trunk, which is the tail mentioned above, extends from $q_z = 0.23$ to about $q_z = 0.26$, and bifurcates into two branches. The intensity of the two branches decreases with increasing $|q_z|$, but the branch between $q_z = 0.26$ to $q_z = 0.33$ is still clearly seen.

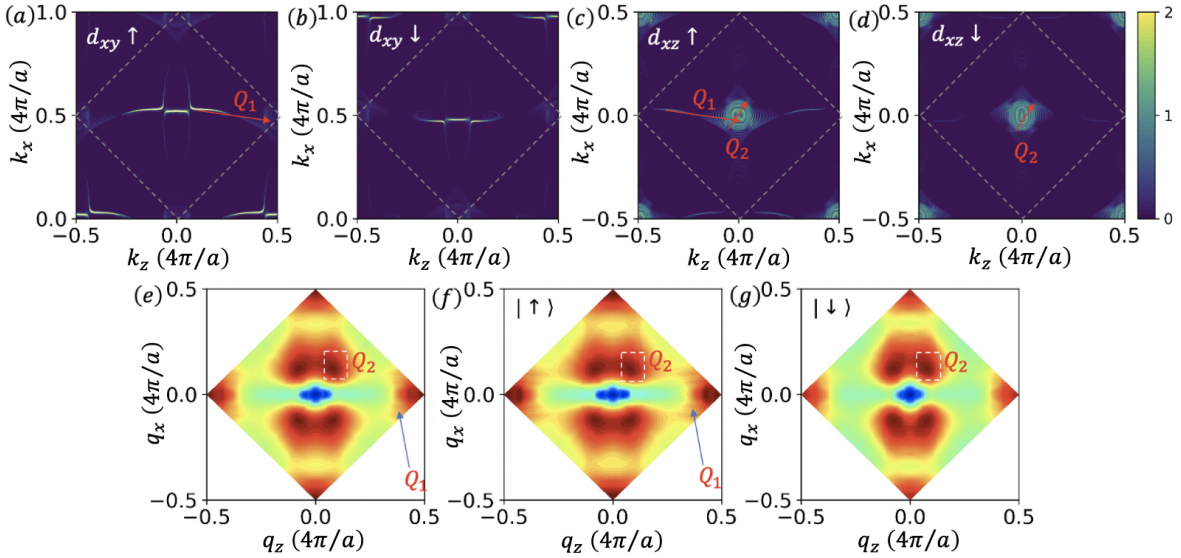

FIG. 8. Spectral functions of (a) spin-up d_{xy}, (b) spin-down d_{xy}, (c) spin-up d_{xz}, and (d) spin-down d_{xz}. (e) total, (f) spin-up and (g) spin-down QPI spectrum.

This bifurcation shaped feature originates from electrons scattered between the shoulder-like portion (denoted by Q') and the slope (marked by Q'') of the Fermi arc, as shown in Fig. 6(b). The enhanced scattering along $q_x = 0$ originates from pure shoulder-shoulder Q' scattering spanning between the mirrored sections of the Fermi arcs. For $q_z > 0.26$, Q'' momentum transfers becomes dominant, tracing out the curvature of the Fermi arc. The intensity of the QPI decreases increased Q'' due to the reduction in the nesting between the shoulder and the curving Fermi arc, therefore, generating the two bifurcating branches in the QPI spectrum.

Figure 7 shows the energy dependence of the Fermi arc I and the bifurcation feature. From panel (a)-(c), we see that as energy increases from -50meV to 50meV, the Fermi arc becomes more curved due to the energetic distance from the Weyl node[50]. This manifests in QPI as a growing angle of the bifurcation branches as shown in Fig. 7(d)-(f).

Ce-site impurity – Now we replace the Bi impurity with a Ce impurity and mark the difference in the surface spectral function and QPI. Here, the d-orbitals play the key role in the Ce impurity induced scattering. We find two noteworthy scattering vectors labeled Q_1 and Q_2 shown in Fig. 8. Q_1 connects the Fermi arcs with trivial bands around Γ. Additionally, because the Ce magnetic moments are along the positive z direction, the spectral function for spin-up d orbitals are more intense than the spin-down d orbitals. As a result, the Q_1 spike-like feature in the total and spin-up QPI spectrum is shown in Fig. 8(e) and 8(f), whereas this feature is not clear in Fig. 8(g). The momentum transfer Q_2, which is similar to Q_4 in the case of Bi impurity, comes from the internal scattering of the bands around the Γ point. This scattering channel is strong for both spin-up and spin-down channels, which makes it a strong feature in all QPI maps.

The features displayed for a Ce impurity are not as rich as those found for a Bi-site scatter because the existence of a dense set of Ce-5d bands surrounding the $\bar{\Gamma}$ point at the Fermi level that generate a significant trivial band scattering background, thus, washing out most features related to Fermi arc scattering in the QPI.

VI. QPI FOR HIGHER ENERGY WEYL NODE

In the previous sections, we have studied the surface states and QPI spectra originating from near the Fermi level of a (010)-oriented slab. Here, we study the surface projected spectral function and QPI map of the (010)-oriented slab for a pair of Weyl nodes above the Fermi level at 0.915 eV, as indicated by the red dashed line in Fig. 9(a). We chose this specific pair of Weyl nodes since they are quite isolated from other intruding bands, which tend to complicate the observation of the Fermi arcs. This Weyl node and the one just below it are both sources of Berry flux as indicated in Fig. 2(a). The surface spectral function at this energy is shown by Fig. 9(b), where two clear wing-like features are found near Γ along the k_x axis. Zooming-in on these features [Fig. 9(c)], it is easy to see that they are Fermi arcs which connect the Weyl nodes. Figure 9(d) shows the σ_3 projection of the spectral function $\langle S_z \rangle$ in the first Brillouin zone, where the red (blue) intensity indicates the strength of the spin-up (spin-down) polarization. Figure 9(e) shows a close-up showing a clear spin texture of the Fermi arc. Similar to our earlier discussion, the scattering between the Fermi arcs with different spin textures can lead to interesting features in the total and spin resolved QPI spectra, as shown in Fig. 9(f), 9(g) and 9(h). Because the spin-up Fermi arcs are curved and the spin-down arcs are relatively

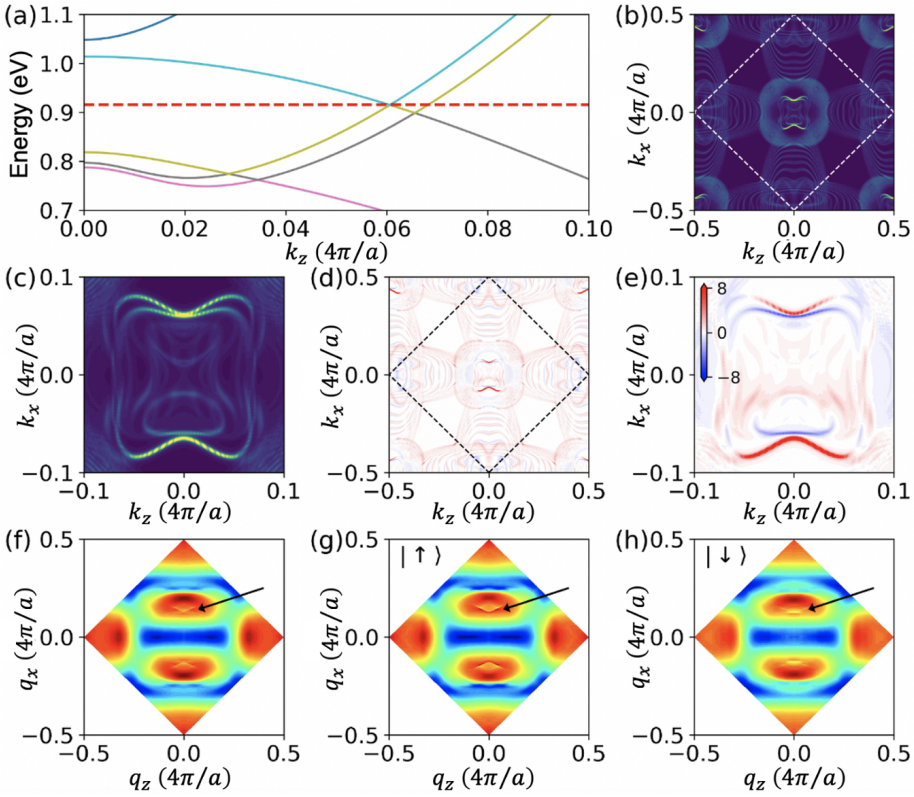

FIG. 9. (a) Theoretical electronic band structure around the Weyl nodes at 0.915 eV. Surface projected spectral function for $\omega = 0.915$ eV in (b) the first Brillouin zone and (c) zoom-in around Γ showing the Fermi arcs. $\langle S_z \rangle$ in (d) the first Brillouin zone and (e) zoom-in around Γ. (f) total, (g) spin-up and (h) spin-down QPI spectra.

flat, the QPI map yields curved and flat features in the spin-up and spin-down QPI spectra, respectively, as indicated by the black arrows. The total QPI also displays a similar curved feature as shown in Fig. 9(f).

VII. CONCLUSION

In summary, we have found theoretically that CeBi is a magnetic Weyl semimetal with two pairs of Weyl nodes close to the Fermi level. The induced two Fermi arcs have opposite spin polarization directions on each surface of a mirror symmetric slab. A nonmagnetic impurity at Bi site can lead to quasiparticle interference pattern with features arising from the Fermi arcs. There is a novel bifurcation shaped feature available in spin-up but absent in spin-down QPI pattern, which is a unique property of this material and can be verified with spin-resolved scanning tunneling probes. Our calculations provide a baseline, from which further experimental and theoretical studies may be initiated to examine the other aspects of Weyl physics in CeBi and other magnetic Weyl materials.

ACKNOWLEDGMENTS

Acknowledgments – We thank Jenny Hoffman for useful discussions. This work was carried out under the auspices of the U.S. Department of Energy (DOE) National Nuclear Security Administration under Contract No. 89233218CNA000001. It was supported by the Center for the Advancement of Topological Semimetals, a DOE BES EFRC. C.L. was supported by LANL LDRD Program. Additional support was provided in part by the Center for Integrated Nanotechnologies, a DOE BES user facility, in partnership with the LANL Institutional Computing Program for computational resources. C.E.M. was supported by the Swiss National Science Foundation under fellowship No. P2EZP2_175155 and P400P2_183890.

* jxzhu@lanl.gov

[1] Xiangang Wan, Ari M. Turner, Ashvin Vishwanath, and Sergey Y. Savrasov, "Topological semimetal and Fermi-arc surface states in the electronic structure of pyrochlore iridates," Phys. Rev. B **83**, 205101 (2011).

[2] Gang Xu, Hongming Weng, Zhijun Wang, Xi Dai, and Zhong Fang, "Chern semimetal and the quantized anomalous hall effect in $HgCr_2Se_4$," Phys. Rev. Lett. **107**, 186806 (2011).

[3] Zhijun Wang, M. G. Vergniory, S. Kushwaha, Max Hirschberger, E. V. Chulkov, A. Ernst, N. P. Ong, Robert J. Cava, and B. Andrei Bernevig, "Time-reversal-breaking Weyl fermions in magnetic heusler alloys," Phys. Rev. Lett. **117**, 236401 (2016).

[4] Noam Morali, Rajib Batabyal, Pranab Kumar Nag, Enke Liu, Qiunan Xu, Yan Sun, Binghai Yan, Claudia Felser, Nurit Avraham, and Haim Beidenkopf, "Fermi-arc diversity on surface terminations of the magnetic Weyl semimetal $Co_3Sn_2S_2$," Science **365**, 1286–1291 (2019).

[5] D. F. Liu, A. J. Liang, E. K. Liu, Q. N. Xu, Y. W. Li, C. Chen, D. Pei, W. J. Shi, S. K. Mo, P. Dudin, T. Kim, C. Cacho, G. Li, Y. Sun, L. X. Yang, Z. K. Liu, S. S. P. Parkin, C. Felser, and Y. L. Chen, "Magnetic Weyl semimetal phase in a kagomé crystal," Science **365**, 1282–1285 (2019).

[6] Ilya Belopolski, Kaustuv Manna, Daniel S. Sanchez, Guoqing Chang, Benedikt Ernst, Jiaxin Yin, Songtian S. Zhang, Tyler Cochran, Nana Shumiya, Hao Zheng, Bahadur Singh, Guang Bian, Daniel Multer, Maksim Litskevich, Xiaoting Zhou, Shin-Ming Huang, Baokai Wang, Tay-Rong Chang, Su-Yang Xu, Arun Bansil, Claudia Felser, Hsin Lin, and M. Zahid Hasan, "Discovery of topological Weyl fermion lines and drumhead surface states in a room temperature magnet," Science **365**, 1278–1281 (2019).

[7] Hongming Weng, Chen Fang, Zhong Fang, B. Andrei Bernevig, and Xi Dai, "Weyl semimetal phase in noncentrosymmetric transition-metal monophosphides," Phys. Rev. X **5**, 011029 (2015).

[8] Su-Yang Xu, Ilya Belopolski, Nasser Alidoust, Madhab Neupane, Guang Bian, Chenglong Zhang, Raman Sankar, Guoqing Chang, Zhujun Yuan, Chi-Cheng Lee, Shin-Ming Huang, Hao Zheng, Jie Ma, Daniel S. Sanchez, BaoKai Wang, Arun Bansil, Fangcheng Chou, Pavel P. Shibayev, Hsin Lin, Shuang Jia, and M. Zahid Hasan, "Discovery of a Weyl fermion semimetal and topological Fermi arcs," Science **349**, 613–617 (2015), https://science.sciencemag.org/content/349/6248/613.full.pdf.

[9] B. Q. Lv, H. M. Weng, B. B. Fu, X. P. Wang, H. Miao, J. Ma, P. Richard, X. C. Huang, L. X. Zhao, G. F. Chen, Z. Fang, X. Dai, T. Qian, and H. Ding, "Experimental discovery of Weyl semimetal TaAs," Phys. Rev. X **5**, 031013 (2015).

[10] Z. K. Liu, L. X. Yang, and et. al., "Evolution of the fermi surface of Weyl semimetals in the transition metal pnictide family," Nature Mater. **15**, 27 (2016).

[11] J. Jiang, Z. Liu, Y. Sun, and et al, "Signature of type-II weyl semimetal phase in $MoTe_2$," Nat. Commun. **8**, 13973 (2017).

[12] L. Huang, T. M. McCormick, and et al, "Spectroscopic evidence for a type II weyl semimetallic state in $MoTe_2$," Nat. Mater. **15**, 1155 (2016).

[13] A. Tamai, Q. S. Wu, I. Cucchi, F. Y. Bruno, S. Riccò, T. K. Kim, M. Hoesch, C. Barreteau, E. Giannini, C. Besnard, A. A. Soluyanov, and F. Baumberger, "Fermi arcs and their topological character in the candidate type-II Weyl semimetal $MoTe_2$," Phys. Rev. X **6**, 031021 (2016).

[14] N. P. Armitage, E. J. Mele, and Ashvin Vishwanath, "Weyl and Dirac semimetals in three-dimensional solids," Rev. Mod. Phys. **90**, 015001 (2018).

[15] A. V. Balatsky, I. Vekhter, and Jian-Xin Zhu, "Impurity-induced states in conventional and unconventional superconductors," Rev. Mod. Phys. **78**, 373–433 (2006).

[16] Hiroyuki Inoue, András Gyenis, Zhijun Wang, Jian Li, Seong Woo Oh, Shan Jiang, Ni Ni, B. Andrei Bernevig, and Ali Yazdani, "Quasiparticle interference of the Fermi arcs and surface-bulk connectivity of a Weyl semimetal," Science **351**, 1184–1187 (2016), https://science.sciencemag.org/content/351/6278/1184.full.pdf.

[17] Hao Zheng, Su-Yang Xu, Guang Bian, Cheng Guo, Guoqing Chang, Daniel S. Sanchez, Ilya Belopolski, Chi-Cheng Lee, Shin-Ming Huang, Xiao Zhang, Raman Sankar, Nasser Alidoust, Tay-Rong Chang, Fan Wu, Titus Neupert, Fangcheng Chou, Horng-Tay Jeng, Nan Yao, Arun Bansil, Shuang Jia, Hsin Lin, and M. Zahid Hasan, "Atomic-scale visualization of quantum interference on a Weyl semimetal surface by scanning tunneling microscopy," ACS Nano **10**, 1378–1385 (2016), pMID: 26743693, https://doi.org/10.1021/acsnano.5b06807.

[18] Rajib Batabyal, Noam Morali, Nurit Avraham, Yan Sun, Marcus Schmidt, Claudia Felser, Ady Stern, Binghai Yan, and Haim Beidenkopf, "Visualizing weakly bound surface Fermi arcs and their correspondence to bulk Weyl fermions," Science Advances **2** (2016), 10.1126/sciadv.1600709, https://advances.sciencemag.org/content/2/8/e1600709.full.pdf.

[19] Paolo Sessi, Yan Sun, Thomas Bathon, Florian Glott, Zhilin Li, Hongxiang Chen, Liwei Guo, Xiaolong Chen, Marcus Schmidt, Claudia Felser, Binghai Yan, and Matthias Bode, "Impurity screening and stability of Fermi arcs against coulomb and magnetic scattering in a Weyl monopnictide," Phys. Rev. B **95**, 035114 (2017).

[20] András Gyenis, Hiroyuki Inoue, Sangjun Jeon, Brian B Zhou, Benjamin E Feldman, Zhijun Wang, Jian Li, Shan Jiang, Quinn D Gibson, Satya K Kushwaha, Jason W Krizan, Ni Ni, Robert J Cava, B Andrei Bernevig, and Ali Yazdani, "Imaging electronic states on topological semimetals using scanning tunneling microscopy," New Journal of Physics **18**, 105003 (2016).

[21] Guoqing Chang, Su-Yang Xu, Hao Zheng, Chi-Cheng Lee, Shin-Ming Huang, Ilya Belopolski, Daniel S. Sanchez, Guang Bian, Nasser Alidoust, Tay-Rong Chang, Chuang-Han Hsu, Horng-Tay Jeng, Arun Bansil, Hsin Lin, and M. Zahid Hasan, "Signatures of Fermi arcs in the quasiparticle interferences of the Weyl semimetals TaAs and NbP," Phys. Rev. Lett. **116**, 066601 (2016).

[22] Pavan Hosur and Xiaoliang Qi, "Recent developments in transport phenomena in Weyl semimetals," Comptes Rendus Physique **14**, 857 – 870 (2013).

[23] Fernando de Juan, Adolfo G. Grushin, Takahiro Morimoto, and Joel E Moore, "Quantized circular photogalvanic effect in Weyl semimetals," Nat. Commun. **8** (2017), https://doi.org/10.1038/ncomms15995 (2017).

[24] Takahiro Morimoto, Shudan Zhong, Joseph Orenstein, and Joel E. Moore, "Semiclassical theory of nonlinear magneto-optical responses with applications to topological Dirac/Weyl semimetals," Phys. Rev. B **94**, 245121 (2016).

[25] A. A. Zyuzin and A. Yu. Zyuzin, "Chiral anomaly and second-harmonic generation in Weyl semimetals," Phys. Rev. B **95**, 085127 (2017).

[26] N. Sirica, R. I. Tobey, L. X. Zhao, G. F. Chen, B. Xu, R. Yang, B. Shen, D. A. Yarotski, P. Bowlan, S. A. Trugman, J.-X. Zhu, Y. M. Dai, A. K. Azad, N. Ni, X. G. Qiu, A. J. Taylor, and R. P. Prasankumar, "Tracking ultrafast photocurrents in the Weyl semimetal TaAs using THz emission spectroscopy," Phys. Rev. Lett. **122**, 197401 (2019).

[27] N. Sirica, P. P. Orth, and et. al., "Photocurrent-driven transient symmetry breaking in the Weyl semimetal TaAs," arXiv:2005,10308 .

[28] A. A. Zyuzin and A. A. Burkov, "Topological response in Weyl semimetals and the chiral anomaly," Phys. Rev. B **86**, 115133 (2012).

[29] M. M. Vazifeh and M. Franz, "Electromagnetic response of Weyl semimetals," Phys. Rev. Lett. **111**, 027201 (2013).

[30] Qiang Li, Dmitri E. Kharzeev, and et. al., "Chiral magnetic effect in $ZrTe_5$," Nature Phys. **12**, 550 (2016).

[31] Tobias Meng and Leon Balents, "Weyl superconductors," Phys. Rev. B **86**, 054504 (2012).

[32] Pavan Hosur, Xi Dai, Zhong Fang, and Xiao-Liang Qi, "Time-reversal-invariant topological superconductivity in doped Weyl semimetals," Phys. Rev. B **90**, 045130 (2014).

[33] He Wang, Huichao Wang, Yuqin Chen, Jiawei Luo, Zhujun Yuan, Jun Liu, Yong Wang, Shuang Jia, Xiong-Jun Liu, Jian Wei, and Jian Wang, "Discovery of tip induced unconventional superconductivity on Weyl semimetal," Science Bulletin **62**, 425 – 430 (2017).

[34] Zhongbo Yan, Zhigang Wu, and Wen Huang, "Vortex end majorana zero modes in superconducting Dirac and Weyl semimetals," Phys. Rev. Lett. **124**, 257001 (2020).

[35] C. Guo, C. Cao, and M. et al. Smidman, "Possible Weyl fermions in the magnetic kondo system CeSb," npj Quant Mater **2**, 39 (2017).

[36] Kenta Kuroda, M. Ochi, H. S. Suzuki, M. Hirayama, M. Nakayama, R. Noguchi, C. Bareille, S. Akebi, S. Kunisada, T. Muro, M. D. Watson, H. Kitazawa, Y. Haga, T. K. Kim, M. Hoesch, S. Shin, R. Arita, and Takeshi Kondo, "Experimental determination of the topological phase diagram in cerium monopnictides," Phys. Rev. Lett. **120**, 086402 (2018).

[37] Paul C. Canfield, "New materials physics," Rep. Prog. Phys. **83**, 016501 (2020).

[38] W. Shon, D.-C. Ryu, K. Kim, B.I. Min, B. Kim, B. Kang, B.K. Cho, H.-J. Kim, and J.-S. Rhyee, "Magnetic field–induced type II Weyl semimetallic state in geometrically frustrated Shastry-Sutherland lattice GdB_4," Materials Today Physics **11**, 100168 (2019).

[39] Peter Blaha, Karlheinz Schwarz, Georg K H Madsen, Dieter Kvasnicka, Joachim Luitz, Robert Laskowsk, Fabien Tran, Laurence Marks, and Laurence Marks, "Wien2k: An augmented plane wave + local orbitals program for calculating crystal properties (Karlheinz Schwarz Techn. Universität Wien, 2019)," (2019).

[40] V. P. Liechtenstein, A. I. and. Antropov and B. N. Harmon, "Electronic structure and magneto-optical effects in CeSb," Phys. Rev. B **49**, 10770 (1994).

[41] Brinda Kuthanazhi, Na Hyun Jo, Li Xiang, Sergey L Bud'ko, and Paul C. Canfield, "Metamagnetism and magnetoresistance in CeBi single crystals," arXiv.1912.08896 (2019).

[42] C. Trainer, C. M. Yim, M. McLaren, and P. Wahl, "Cryogenic stm in 3d vector magnetic fields realized through a rotatable insert," Review of Scientific Instruments **88**, 093705 (2017), https://doi.org/10.1063/1.4995688.

[43] Jan Kuneš, Ryotaro Arita, Philipp Wissgott, Alessandro Toschi, Hiroaki Ikeda, and Karsten Held, "Wien2wannier: From linearized augmented plane waves to maximally localized wannier functions," Computer Physics Communications **181**, 1888 – 1895 (2010).

[44] Roxanne M. Tutchton, Wei-ting Chiu, R. C. Albers, G. Kotliar, and Jian-Xin Zhu, "Electronic correlation induced expansion of fermi pockets in δ-plutonium," Phys. Rev. B **101**, 245156 (2020).

[45] Dong-Choon Ryu, Junwon Kim, Kyoo Kim, Chang-Jong Kang, J. D. Denlinger, and B. I. Min, "Distinct topological properties in ce monopnictides having correlated f electrons: CeN vs. CeBi," Phys. Rev. Research **2**, 012069 (2020).

[46] QuanSheng Wu, ShengNan Zhang, Hai-Feng Song, Matthias Troyer, and Alexey A. Soluyanov, "WannierTools : An open-source software package for novel topological materials," Comput. Phys. Commun. **224**, 405–416 (2018), arXiv:1703.07789 [physics.comp-ph].

[47] Xinjie Wang, Jonathan R. Yates, Ivo Souza, and David Vanderbilt, "Ab initio calculation of the anomalous hall conductivity by wannier interpolation," Phys. Rev. B **74**, 195118 (2006).

[48] Di Xiao, Ming-Che Chang, and Qian Niu, "Berry phase effects on electronic properties," Rev. Mod. Phys. **82**, 1959–2007 (2010).

[49] M P Lopez Sancho, J M Lopez Sancho, J M L Sancho, and J Rubio, "Highly convergent schemes for the calculation of bulk and surface green functions," Journal of Physics F: Metal Physics **15**, 851–858 (1985).

[50] "See supplemental material for more details," .

[51] Sooyoung Jang, Robert Kealhofer, Caolan John, Spencer Doyle, Ji-Sook Hong, Ji Hoon Shim, Q. Si, O. Erten, Jonathan D. Denlinger, and James. G. Analytis, "Direct visualization of coexisting channels of interaction in CeSb," Science Advances **5** (2019), 10.1126/sciadv.aat7158, https://advances.sciencemag.org/content/5/3/eaat7158.full.pdf.

Supplemental Material for "Prediction of Spin Polarized Fermi Arcs in Quasiparticle Interference of CeBi"

Zhao Huang,[1] Christopher Lane,[1,2] Chao Cao,[3] Guo-Xiang Zhi,[4] Yu Liu,[5] Christian E. Matt,[5] Brinda Kuthanazhi,[6,7] Paul C. Canfield,[6,7] Dmitry Yarotski,[2] A. J. Taylor,[2] and Jian-Xin Zhu[1,2,*]

[1]*Theoretical Division, Los Alamos National Laboratory, Los Alamos, New Mexico 87545, USA*
[2]*Center for Integrated Nanotechnology, Los Alamos National Laboratory, Los Alamos, New Mexico 87545, USA*
[3]*Department of Physics, Hangzhou Normal University, Hangzhou 310036, China*
[4]*Department of Physics, Zhejiang University, Hangzhou 310013, China*
[5]*Department of Physics, Harvard University, Cambridge, Massachusetts 02138, USA*
[6]*Ames Laboratory, Iowa State University, Ames, Iowa 50011, USA*
[7]*Department of Physics and Astronomy, Iowa State University, Ames, Iowa 50011, USA*

(Dated: January 22, 2022)

arXiv:2008.10628v3 [cond-mat.str-el] 14 Jan 2021

FORMULA OF QUASIPARTICLE INTERFERENCE

In this section we derive the expression for the quasiparticle interference for the surface layer of a slab with two atoms A and B in a primitive cell. The location of all atoms on the surface is given by an in-plane vector $\mathbf{r_i}$, where *i even* denotes the A sublattice and *i odd* gives the B sublattice. The Green's function of the entire slab with an impurity at site $\mathbf{r_1}$ (type B) is given by

$$\Sigma_{j'}[i\omega_n\delta_{ij'}\mathbf{I}-\mathbf{h}_{\mathrm{ij'}}]\mathbf{G}(\mathrm{j',j})=\delta_{\mathrm{ij}}\mathbf{I}+\mathbf{V}_{\mathrm{imp}}\delta_{i1}\mathbf{G}(1,\mathrm{j}), \tag{S1}$$

where i, j, j' index the atom locations throughout the entire slab, $\mathbf{h}_{\mathrm{ij'}}$ is the hopping matrix connecting orbitals in unit cell i to those in unit cell j', and $\mathbf{V}_{\mathrm{imp}}$ is the impurity potential matrix. Moreover, $\mathbf{V}_{\mathrm{imp}}$ is block diagonal in atomic species, with only a 6 by 6 nonzero block for B-type vacancy only composed of 3 Bi-6p orbitals plus spin. This means if the A site is composed of 5 Ce-5d orbitals plus spin degrees of freedom, the overall dimension of $\mathbf{I}$, $\mathbf{h}, \mathbf{G}$ and $\mathbf{V}_{\mathrm{imp}}$ can grow rapidly for increased number of layers. Then by defining the Green's function in the pristine case

$$\Sigma_{j'}[i\omega_n\delta_{ij'}\mathbf{I}-\mathbf{h}_{\mathrm{ij'}}]\mathbf{G}_0(\mathrm{j',j})=\delta_{\mathrm{ij}}\mathbf{I}, \tag{S2}$$

we can write the full greens function in terms of the $\mathbf{T_{imp}}$ matrix,

$$\mathbf{G}(\mathrm{i,j})=\mathbf{G}_0(\mathrm{i,j})+\mathbf{G}_0(\mathrm{i},1)\mathbf{T}_{\mathrm{imp}}\mathbf{G}_0(1,\mathrm{j}), \tag{S3}$$

where $\mathbf{T_{imp}}$ is obtained as

$$\mathbf{T}_{\mathrm{imp}}=\mathbf{V}_{\mathrm{imp}}(I-\mathbf{G}_0(1,1)\mathbf{V}_{\mathrm{imp}})^{-1}. \tag{S4}$$

If we only consider the first Born approximation, where $V_{imp} \ll 1$, the deviations from $\mathbf{G}_0$ can be written as

$$\delta\mathbf{G}(\mathrm{i,i})=\mathbf{G}_0(\mathrm{i},1)\mathbf{V}_{\mathrm{imp}}\mathbf{G}_0(1,\mathrm{i})\ . \tag{S5}$$

This determines the corresponding local density of states for sites A and B,

$$\rho(2i)=-\frac{1}{\pi}\mathrm{ImTr}[\mathbf{G}_0(2\mathrm{i},1)\mathbf{V}_{\mathrm{imp}}\mathbf{G}_0(1,2\mathrm{i})], \tag{S6}$$

$$\rho(2i+1)=-\frac{1}{\pi}\mathrm{ImTr}[\mathbf{G}_0(2\mathrm{i}+1,1)\mathbf{V}_{\mathrm{imp}}\mathbf{G}_0(1,2\mathrm{i}+1)]. \tag{S7}$$

Since we only wish to examine the QPI spectrum relevant to STM measurements, we restrict $\mathbf{G}_0$ to just surface atomic sites. Therefore, we define the surface local density of states for sites A and B as

$$\rho_s(2i)=-\frac{1}{\pi}\mathrm{ImTr}[\mathbf{G}_{\mathrm{s0}}(2\mathrm{i},1)\mathbf{V}_{\mathrm{p}}\mathbf{G}_{\mathrm{s0}}(1,2\mathrm{i})], \tag{S8}$$

$$\rho_s(2i+1)=-\frac{1}{\pi}\mathrm{ImTr}[\mathbf{G}_{\mathrm{s0}}(2\mathrm{i}+1,1)\mathbf{V}_{\mathrm{p}}\mathbf{G}_{\mathrm{s0}}(1,2\mathrm{i}+1)], \tag{S9}$$

where G_{s0} is the surface Green function with a dimension of 10×6 or 6×10 (6×6) for site A (B), and $\mathbf{V}_{\rm p}$ is the nonzero 6×6 block of $\mathbf{V}_{\rm imp}$. Since we have periodic boundary conditions in the xy plane of the slab geometry, we are able to perform Fourier transform to obtain the quasiparticle interference spectral function at the surface as

$$\rho_{sA}(\mathbf{q}) = \sum_i \rho_s(2i)\exp(-i\mathbf{q}\cdot\mathbf{r}_{2i}), \tag{S10}$$

$$\mathbf{G}_{s0}(2i,1) = \langle d_{2i}p_1^\dagger\rangle = \sum_{\mathbf{k}} \mathbf{G}_{s0}^{dp}(\mathbf{k})\exp(i\mathbf{k}\cdot(\mathbf{r}_{2i}-\mathbf{r}_1)) \ \text{ with } \ \mathbf{G}_{s0}^{dp}(\mathbf{k}) = \langle d_{\mathbf{k}}p_{\mathbf{k}}^\dagger\rangle, \tag{S11}$$

$$\mathbf{G}_{s0}(1,2i) = \langle p_1 d_{2i}^\dagger\rangle = \sum_{\mathbf{k}} \mathbf{G}_{s0}^{pd}(\mathbf{k})\exp(-i\mathbf{k}\cdot(\mathbf{r}_{2i}-\mathbf{r}_1)) \ \text{ with } \ \mathbf{G}_{s0}^{pd}(\mathbf{k}) = \langle p_{\mathbf{k}}d_{\mathbf{k}}^\dagger\rangle, \tag{S12}$$

$$\rho_{sB}(\mathbf{q}) = \sum_i \rho_s(2i+1)\exp(-i\mathbf{q}\cdot\mathbf{r}_{2i+1}), \tag{S13}$$

$$\mathbf{G}_{s0}(2i+1,1) = \langle p_{2i+1}p_1^\dagger\rangle = \sum_{\mathbf{k}} \mathbf{G}_{s0}^{pp}(\mathbf{k})\exp[i\mathbf{k}\cdot(\mathbf{r}_{2i+1}-\mathbf{r}_1)] \ \text{ with } \ \mathbf{G}_{s0}^{pp}(\mathbf{k}) = \langle p_{\mathbf{k}}p_{\mathbf{k}}^\dagger\rangle, \tag{S14}$$

$$\mathbf{G}_{s0}(1,2i+1) = \sum_{\mathbf{k}} \mathbf{G}_{s0}^{pp}(\mathbf{k})\exp[-i\mathbf{k}\cdot(\mathbf{r}_{2i+1}-\mathbf{r}_1)]. \tag{S15}$$

Combining Eqs. (S8), (S10), (S11) and (S12), we arrive at

$$\rho_{sA}(\mathbf{q}) = \sum_i -\frac{1}{\pi}\mathrm{ImTr}[\mathbf{G}_{s0}(2i,1)\mathbf{V}_{\rm p}\mathbf{G}_{s0}(1,2i)]\exp(-i\mathbf{q}\cdot\mathbf{r}_{2i}) \tag{S16}$$

$$= \frac{i}{2\pi}\sum_i\sum_{k,k'}\mathrm{Tr}[\mathbf{G}_{s0}^{dp}(\mathbf{k})\mathbf{V}_{\rm imp}\mathbf{G}_{s0}^{pd}(\mathbf{k}')\exp[i(\mathbf{k}-\mathbf{k}')\cdot(\mathbf{r}_{2i}-\mathbf{r}_1)] - c.c.]\exp(-i\mathbf{q}\cdot\mathbf{r}_{2i}) \tag{S17}$$

$$= \frac{i}{2\pi}\sum_k \mathrm{Tr}[\mathbf{G}_{s0}^{dp}(\mathbf{k})\mathbf{V}_{\rm imp}\mathbf{G}_{s0}^{pd}(\mathbf{k}-\mathbf{q}) - [\mathbf{G}_{s0}^{dp}(\mathbf{k})\mathbf{V}_{\rm p}\mathbf{G}_{s0}^{pd}(\mathbf{k}+\mathbf{q})]^*]\exp(-i\mathbf{q}\cdot\mathbf{r}_1), \tag{S18}$$

and combining Eq. (S9), (S13), (S14) and (S15) we find

$$\rho_{sB}(\mathbf{q}) = \sum_i -\frac{1}{\pi}\mathrm{ImTr}[\mathbf{G}_{s0}(2i+1,1)\mathbf{V}_{\rm p}\mathbf{G}_{s0}(1,2i+1)]\exp(-i\mathbf{q}\cdot\mathbf{r}_{2i+1}) \tag{S19}$$

$$= \frac{i}{2\pi}\sum_i\sum_{k,k'}\mathrm{Tr}[\mathbf{G}_{s0}^{pp}(\mathbf{k})\mathbf{V}_{\rm p}\mathbf{G}_{s0}^{pp}(\mathbf{k}')\exp[i(\mathbf{k}-\mathbf{k}')\cdot(\mathbf{r}_{2i+1}-\mathbf{r}_1)] - c.c.]\exp(-i\mathbf{q}\cdot\mathbf{r}_{2i+1}) \tag{S20}$$

$$= \frac{i}{2\pi}\sum_k \mathrm{Tr}[\mathbf{G}_{s0}^{pp}(\mathbf{k})\mathbf{V}_{\rm p}\mathbf{G}_{s0}^{pp}(\mathbf{k}-\mathbf{q}) - [\mathbf{G}_{s0}^{pp}(\mathbf{k})\mathbf{V}_{\rm p}\mathbf{G}_{s0}^{pp}(\mathbf{k}+\mathbf{q})]^*]\exp(-i\mathbf{q}\cdot\mathbf{r}_1). \tag{S21}$$

To make the above expression more computationally tractable, we drop the common factor $\exp(-i\mathbf{q}\cdot\mathbf{r}_1)$ for ρ_{sA} and ρ_{sB}. Additionally, since $\mathbf{V}_{\rm imp} = V\mathbf{I}$ for an isotropic nonmagnetic impurity we find

$$\rho_{sA}(\mathbf{q}) = \frac{i}{2\pi}V\sum_k \mathrm{Tr}[\mathbf{G}_{s0}^{dp}(\mathbf{k}+\mathbf{q})\mathbf{G}_{s0}^{pd}(\mathbf{k})] - \mathrm{Tr}[\mathbf{G}_{s0}^{dp}(\mathbf{k})\mathbf{G}_{0}^{pd}(\mathbf{k}+\mathbf{q})]^* \tag{S22}$$

$$= \frac{i}{2\pi}V\sum_k \mathrm{Tr}[\mathbf{G}_{s0}^{dp}(\mathbf{k}+\mathbf{q})\mathbf{G}_{s0}^{pd}(\mathbf{k})] - \mathrm{Tr}[\mathbf{G}_{0}^{dp}(\mathbf{k})\mathbf{G}_{s0}^{pd}(\mathbf{k}+\mathbf{q})]^* \tag{S23}$$

and

$$\rho_{sB}(\mathbf{q}) = \frac{i}{2\pi}V\sum_k \mathrm{Tr}[\mathbf{G}_{s0}^{pp}(\mathbf{k}+\mathbf{q})\mathbf{G}_{s0}^{pp}(\mathbf{k})] - \mathrm{Tr}[\mathbf{G}_{s0}^{pp}(\mathbf{k})\mathbf{G}_{s0}^{pp}(\mathbf{k}+\mathbf{q})]^* \tag{S24}$$

$$= -\frac{1}{\pi}V\sum_k \mathrm{TrIm}[\mathbf{G}_{s0}^{pp}(\mathbf{k}+\mathbf{q})\mathbf{G}_{s0}^{pp}(\mathbf{k})]. \tag{S25}$$

Finally, the total spectral function is

$$\mathrm{B}(\mathbf{q}) = \rho_{sA}(\mathbf{q}) + \rho_{sB}(\mathbf{q}). \tag{S26}$$

In many cases, the off-diagonal contribution ρ_{sA} is much smaller than ρ_{sB}. It is a good approximation to just keep only $\rho_{sB}(\mathbf{q})$) in $B(\mathbf{q})$ [**?**]. In our case, because ρ_{sA} is comparable with ρ_{sB} for some $\mathbf{q}$, we still take the Eq. (S26) to calculate the QPI spectra.

SURFACE ELECTRONIC STRUCTURE AND QPI OF (001)-ORIENTED SURFACE

In the following we compare our calculated surface spectral function and corresponding theoretically predicted QPI intensity with experimental results on the (001)-oriented surface, which is orthogonal to the (010)-oriented surface presented in the main manuscript. Due to technical limitations – the available in-plane magnetic field is limited to 3 Tesla – our QPI calculations and predictions of Fermi arcs on the (010)-oriented surface cannot be directly confirmed by experiments. However, the good agreement between our calculations and experiments on the (001)-oriented surface confirms and validates our methodology and calculations.

We have calculated the surface spectral function and the Bi vacancy induced QPI spectra at $\omega = -100$ meV and -200 meV. Figure S1 compares our theoretically obtained QPI spectra to experimental results. In our theoretical spectral functions [Fig. S1(a) and S1(d)] no Fermi arc is present due to the absence of xy-mirror symmetry in the (001)-oriented slab. Rather, a trivial cross-like Fermi surface pocket surrounding $\bar{M}$ and weak weight near $\bar{\Gamma}$ is present. In the corresponding QPI maps [Fig. S1(b) and S1(e)] the main scattering peak around $\mathbf{q} = 0$ is circular for $\omega = -100$ meV, but transforms in to a rectangle for $\omega = -200$ meV.

In our experiments, using scanning tunneling spectroscopy (STS) we measured QPI on the (001)-oriented surface of CeBi in the FM-like state at 4 K (see Figs. S1 (c), (f)). Single crystals of CeBi were grown out of a Bi-rich binary melt with an initial composition of $Ce_{26}Bi_{74}$ [**?**]. Elemental Ce and Bi were placed in a 3-cap-Ta crucible [**?**] and slowly cooled from 1200 °C to 940 °C over 60 hours. Once at 940 °C the excess solution was decanted from the CeBi single crystals with the aid of a centrifuge [**?**]. CeBi samples were then cleaved in cryogenic, ultrahigh vacuum at 30 K before inserting them into the STM head. The Ce magnetic moments are fully aligned by a 9 Tesla external magnetic fields applied along the c-axis. By overlaying the key features of our theoretical results on top of the experimental QPI spectra [Fig. S1(c) and S1(f)] we find reasonable agreement. For the case of $\omega = -100$ meV, the theoretical and experimental results both have a circular high intensity peak around $\bar{\Gamma}$. Theory and experimental QPI is also consistent for the intense scattering near the corners of the Brillouin zone marked by a dashed red curve. For $\omega = -200$ meV, we find the same level of agreement between theory and experiment, where the size of the predicted and measured rectangle around $\bar{\Gamma}$ almost exactly the same.

By considering an isotropic nonmagnetic impurity potential at the Bi site, we obtain theoretical results in good accord with the experimentally observed QPI. This suggests that Bi vacancies at the surface of CeBi behave as isotropic nonmagnetic impurities. Therefore, the T-matrix approximation $\mathbf{T} = \mathbf{V_{imp}}$ is reasonable and produces realistic results.

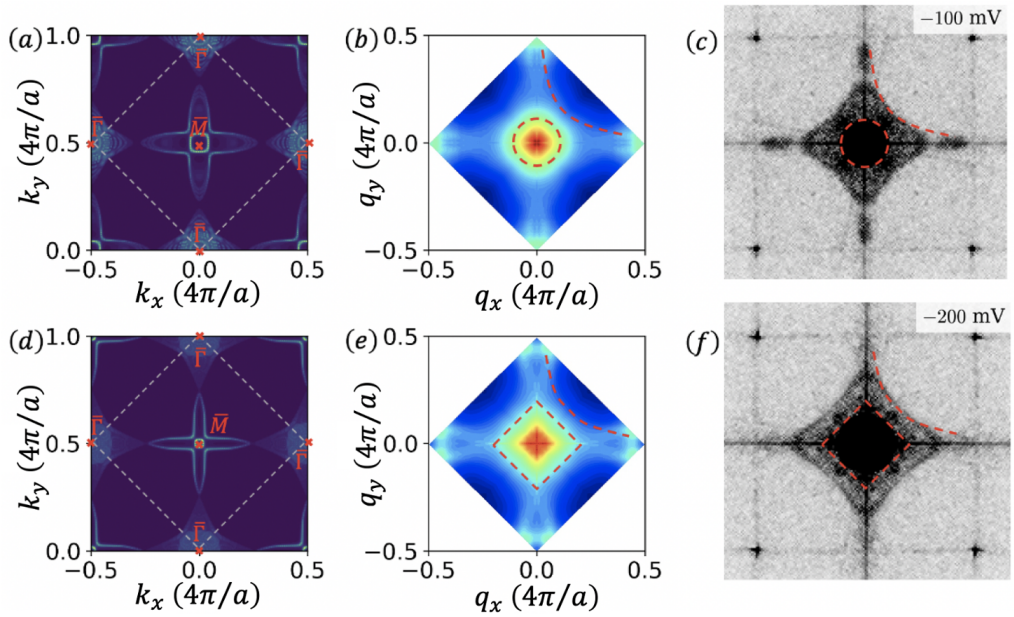

FIG. S1: Surface projected spectral function for (a) $\omega = -100$ meV and (d) $\omega = -200$ meV. QPI spectra for a single Bi impurity for (b) $\omega = -100$ meV and (e) $\omega = -200$ meV. Experimental QPI map measured at (c) −100mV and (f) −200mV bias voltages. Setup parameters for the QPI maps (c) and (f) are $V_s = 200$ mV, $R_J = 0.4$ GΩ, where V_s denotes the sample bias and R_J the tunneling junction resistance. The bias excitation amplitude was set to $V_{\rm rms} = 7.1$ mV.

TOPOLOGICAL NONTRIVIAL AND TRIVIAL SURFACE BANDS

To show the band dispersions related to the Fermi arcs, we calculated the band structures of a 30-layer (010) slab with respect to k_x for a list of k_z as shown in Fig. S2. Both the open and closed boundary conditions are considered to distinguish the nontrivial surface band. We can see several features by comparing these panels. 1) Energy bands with linear dispersions are available in panel (a), (c), (e) and (g) but absent in (b), (d), (f) and (h). This means the existence of nontrivial massless bands at the open surface, which form the Fermi arcs. The bands have small gaps thus not perfectly massless because the finite depth of the slab. 2) We can see two linear-dispersion bands in (i) ($k_z = 0.2$) but only one in (k) ($k_z = 0.25$), which indicates a Weyl node between $k_z = 0.2$ and 0.25 because the 2D momentum plane between a pair of Weyl nodes has a nonzero Chern number [**?**]. 3) For the same reason, one linear-dispersion band in (k) but none in (m) indicates another Weyl node between $k_z = 0.25$ and 0.3.

The energy cuts on bands in Fig. S2 correspond to the peaks in the map of spectral functions as shown in Fig. S3. Specifically, the cuts on the bands with linear dispersion form the Fermi acrs. Fig. S3(h)-(n) show the exchange of red and blue band (Fermi arcs) around the central area. This exchange is due to crossing of the massless linear bands shown in Fig. S2.

* Electronic address: jxzhu@lanl.gov

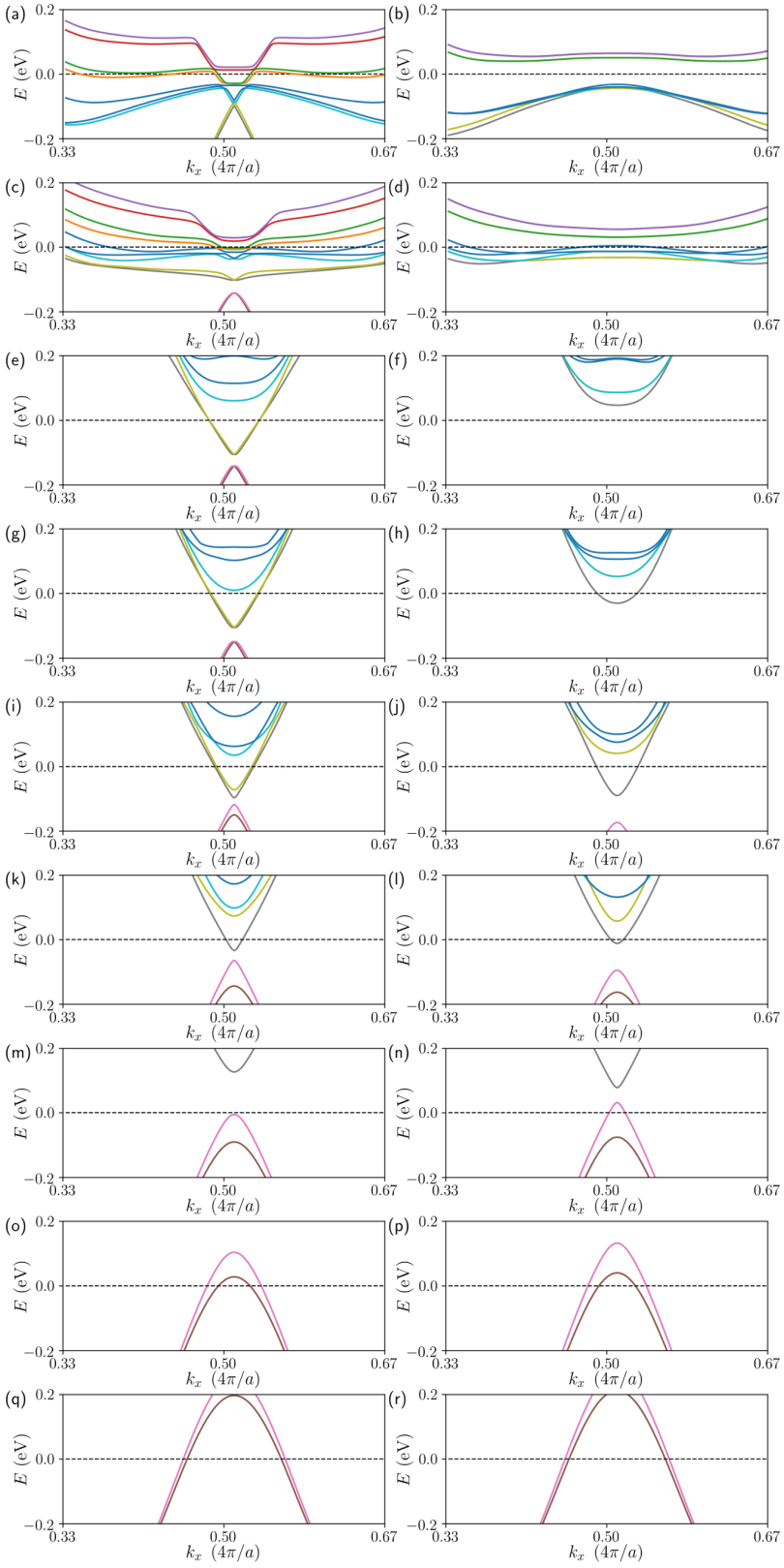

FIG. S2: Band structures of a 30-layer (010) slab with open and closed boundary condition in the y-direction for various values of k_z. k_z = 0, 0.05, 0.1, 0.15, 0.2, 0.25, 0.3, 0.35 and 0.4 for panels from the first to the last row. The boundary condition is open and closed for panels in the left and right column.

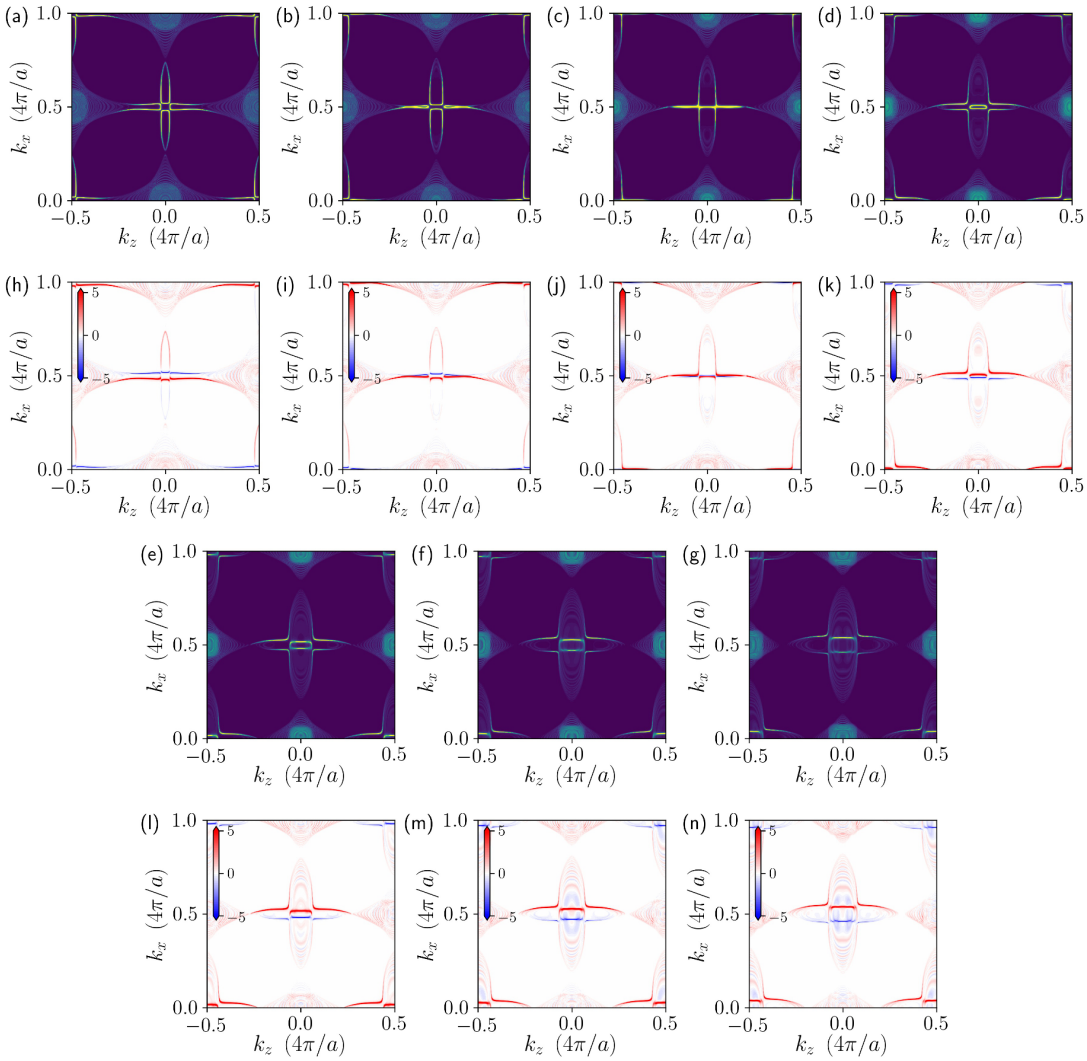

FIG. S3: (a) - (g) Surface spectral function of a (010)-oriented slab at $E = -0.2,\ -0.15,\ -0.1,\ -0.05,\ 0,\ 0.05$ and 0.1 eV. (h) - (n) Spectral functions for spin polarization $\langle S_z \rangle$ at $E = -0.2,\ -0.15,\ -0.1,\ -0.05,\ 0,\ 0.05$ and 0.1 eV.